International Journal of Nanomedicine Dovepress

Open Access Full Text Article ORIGINAL RESEARCH

Chitosan/Sodium Tripolyphosphate/Sodium Alginate/miRNA-34c-5p Antagomir Scaffolds Promote the Functionality of Rabbit Cranial Parietal Repair

Chen Lin[1,2], Xinyi Bai[3], Linkun Zhang[1,2]

[1]Department of Orthodontics, Tianjin Stomatological Hospital, School of Medicine, Nankai University, Tianjin, 300041, People's Republic of China; [2]Tianjin Key Laboratory of Oral and Maxillofacial Function Reconstruction, Tianjin, 300041, China; [3]Department of Stomatology, Beijing Shunyi District Hospital, Beijing, 101300, People's Republic of China

Correspondence: Linkun Zhang, Department of Orthodontics, Tianjin Stomatological Hospital, School of Medicine, Nankai University, Tianjin, 300041, People's Republic of China, Email linkunzhang@nankai.edu.cn

Purpose: MicroRNA-34c-5p (miR-34c-5p) plays a pivotal role in bone remodeling, yet its therapeutic potential is hindered by challenges such as instability, limited cellular internalization, and immune responses. This study was aimed at developing innovative scaffolds capable of efficiently delivering microRNAs (miRNAs), specifically miR-34c-5p.

Methods: Chitosan (CS)/sodium tripolyphosphate (STPP)/sodium alginate (SA) scaffolds, referred to as CTS scaffolds, were synthesized at a specific ratio and characterized using dynamic light scattering and scanning electron microscopy (SEM). Cytotoxicity assessments were conducted through cell activity staining. The loading capacity and releasing performance of miRNAs were quantified using spectrophotometry. Subsequently, the in vivo efficacy of miR-34c-5p Agomir/Antagomir in regulating bone repair was evaluated in the rabbit cranial bone defect model, with micro-CT scanning and histological analysis conducted at 4, 8, and 12 weeks.

Results: CTS scaffolds with a composition ratio of 1:0.2:0.1 were successfully synthesized, exhibiting a mean particle size of 360.1 nm. SEM revealed scaffolds had the porous spongy structure. Cell activity staining confirmed the excellent biocompatibility of the CTS scaffolds. Spectrophotometry demonstrated miR-34c-5p Antagomir were continually released, reaching 91.41% within 30 days. Differential new bone formation was observed between the miR-34c-5p Agomir and Antagomir groups. Micro-CT imaging and histological staining revealed varying degrees of bone regeneration, with notable improvements in the miR-34c-5p Antagomir group.

Conclusion: CTS scaffolds with a composition ratio of 1:0.2:0.1 demonstrate favorable biocompatibility and enable efficient loading and sustained release of miR-34c-5p Antagomir. The study suggests potential applications of miR-34c-5p Antagomir in promoting bone repair and highlights the promise of innovative scaffolds for therapeutic miRNAs administration in bone regeneration.

Keywords: microRNA, scaffold, bone remodeling, chitosan

Introduction

MicroRNAs (miRNAs) play a crucial role in cell functions such as proliferation, apoptosis and regulating differentiation on mesenchymal stem cells.[1–3] Meanwhile, miRNAs have been shown to significantly alter protein expression levels in bone remodeling. Previous studies indicated exosome-mediated miRNAs can be delivered to recipient cells. Of particular interest is miR-34c-5p, which has been implicated in various aspects of bone remodeling. For instance, miR-34c-5p was found to be up-regulated in PGE_2-induced exosomes derived from periodontal ligament cells, exerting the notable influence on bone remodeling through the MDM4 pathway.[4] Furthermore, recent studies have highlighted the involvement of miR-34c-5p in regulating the lipogenic differentiation on bone marrow mesenchymal stem cells,[5] as well as in the proliferation and differentiation on periodontal ligament stem cells.[6] Additionally, miR-34c plays a pivotal role in osteogenic differentiation, impacting both dental pulp and bone marrow stem cells.[7] Our previous research contributed to demonstrate that exosomal

Received: 8 June 2024
Accepted: 22 November 2024
Published: 2 December 2024

miR-34c-5p inhibits osteogenic differentiation on periodontal ligament stem cells via the SATB2/ERK pathway.[8] Given these findings, miR-34c-5p emerges as a potential target for modulating bone remodeling processes.

Given the potential of exogenous miRNA mimics for bone tissue regeneration, it is crucial to develop suitable scaffolds that can efficiently carry and deliver these miRNAs to the target bone tissue.[9] However, several technical challenges and safety concerns need to be addressed, including the short half-life and degradation of miRNAs in the bloodstream. These issues pose significant hurdles in the application of miRNAs for in situ bone defect regeneration.[10,11] To overcome these challenges, researchers have been focusing on developing platforms that can accumulate miRNAs at specific sites of interest, achieving tissue-specific targeting. Over the past decade, various advanced scaffolds have been designed for bone regeneration, with the microporous framework that mimics the physical characteristics of the extracellular matrix and supports cell adhesion, migration, and morphogenesis.[12] Among these scaffolds, porous scaffolds are considered more suitable for drug delivery systems due to their ability to provide a stable and controlled release of therapeutic agents.[13] To address the delivery of miRNAs, various strategies have been attempted. Zhang et al demonstrated the stabilizing effect of extracellular vesicles on miRNAs, which offered the promising approach for in vivo miRNA research.[14] Additionally, the novel in-situ nano-composite hydrogel with ROS-controlled drug release had been developed for the repair of irregular cartilage defects. This hydrogel effectively promoted the regeneration of rat articular cartilage defects, highlighting the potential of controlled release systems in tissue regeneration.[15]

Chitosan (CS) is the natural polysaccharide with positively charged properties,[16] has shown great potential in forming nanoscale complexes with negatively charged nucleic acids such as siRNAs and miRNAs.[17,18] This unique interaction allows CS to serve as a non-viral vector for the delivery of therapeutic nucleic acids. Sodium tripolyphosphate (STPP) is another key component in the preparation of vector-carrying due to its good biocompatibility and ability to induce collagen mineralization.[19] Nanoparticles can be prepared by ion crosslinking between positively charged CS and negatively charged STPP. The current research showed that plasmid DNA, siRNAs, miRNAs, proteins and anticancer drugs can be delivered safely by chitosan-based non-viral vectors.[20,21] In this study, the novel scaffold composed of CS, STPP, and Sodium alginate (SA) was developed for the delivery of miRNAs. In animal experiments, the rabbit cranioparietal critical-sized defect (CSD) model was always used to evaluate assessment of biocarrier materials and cell-free therapies in the minimally invasive and non-healing defect environment.[22,23]

The present study aims to further explore the therapeutic potential of miR-34c-5p by developing the novel delivery system that can efficiently transport miRNAs, with its impact on bone repair and regeneration. Additionally, the rabbit cranioparietal CSD model was adopted to assess the therapeutic impact of miR-34c-5p Agomir and Antagomir. We expect this novel design would find an original, effective strategy for new advancements in therapeutic nucleic acid delivery and tissue regeneration.

Material and Methods

Materials

CS of 100 kDa with a 90% deacetylation degree was procured from Aladdin Co., Ltd. (Shanghai, China). STPP was sourced from Wanvi (Shanghai, China); meanwhile, SA was obtained from Solarbio (Beijing, China). The miR-34c-5p Agomir (5'-AGGCAGUGUAGUUAGCUGA-3') and miR-34c-5p Antagomir were acquired from Sangon Biotech Co., Ltd. (Shanghai, China).

Preparation of CTS/miR-34c-5p Nanoparticles

The scaffolds were prepared by the mixture of different CS/STPP/SA (CTS) volume ratios (①1:0.1:0.02; ②1:0.2:0.02;③1:0.2:0.05;④1:0.2:0.1;⑤1:0.2:0.5). 1 g CS (1%, w/v) was dissolved in 0.1 M acetic acid solution to obtain 1 mg/mL CS-acetic acid solution. STPP (1 mg/mL) and SA (1 mg/mL) were mixed in ultra-pure water and filtered with the 0.22 μm membranes. The pre-mixed STPP/SA solution with different volume ratios was added to the CS solution dropwise and stirred for 2 h to form the fixed nano-particles (NPs) of CTS. For the preparation of the scaffolds, 100 μL of each CTS mixture was pipetted onto a 96-well plate and spread as evenly as possible to eliminate bubbles. The mixtures were then frozen at −20°C for 24 h and subsequently freeze-dried for 9 h to form loose porous scaffolds. Prior

to experimentation, the scaffolds were sterilized at 110°C for 30 mins. To form the complex, 5 nmol of miR-34c-5p Antagomir solution was added to the CTS scaffolds at a molar ratio of N/P=20:1 (N/P, refers to positive amino groups in CS versus negatively charged phosphate groups in miRNA).

Characterization of CTS/miR-34c-5p NPs

The diameter and polymer dispersity index (PDI) of the CTS scaffolds were measured using the NS300 nano-size analyzer (Malvern, UK). These measurements were taken at a temperature of 25°C, with a detection angle of 90° and a wavelength of 488 nm (blue).

To determine the water absorption of the CTS scaffolds, scaffolds with different ratios were placed in ultra-pure water overnight. Prior to measurement, any surface moisture was removed using filter paper, and the mass of the scaffolds was recorded as M1. Subsequently, the scaffolds from each group were vacuum dried for 9 h, and their mass was recorded as M2. The water absorption expansion rate was calculated using the formula: (M1-M2)/M2×100%.

The porosity of the scaffolds was evaluated using the modified liquid displacement method. First, anhydrous ethanol was poured into a measuring cylinder, and the initial volume was noted as V1. The freeze-dried scaffold was then immersed in the ethanol for 5 minutes, and the volume of the ethanol after immersion was recorded as V2. After removing the scaffold, the residual volume of the ethanol was measured as V3. The porosity of the scaffolds for each group was calculated using the following formula: (V1-V3)/(V2-V3)×100%. These measurements and calculations were used to guide the selection of the optimal formulation ratio among the different groups.

The morphology of freeze-dried CTS scaffold was observed by SEM (Zeiss Gemini 300) at room temperature after sputter coating with gold on copper grids. By examining the scaffolds under the SEM, detailed information about their structure and surface features can be obtained.

Cytotoxicity and miRNA Transfection

The MC3T3-E1 cell line, used for in vitro experiments, was sourced from Procell (Wuhan, China). Cells were cultured in α-MEM medium (Gibco, Invitrogen, USA), supplemented with 15% fetal bovine serum (TIANHANG, China). The cytotoxic effect of the scaffolds on MC3T3-E1 cells was assessed using the live/dead cell staining kit (Beyotime, China). MC3T3-E1 cells were inoculated in 24-well plates and divided into two groups. (i) Control group: normal culture for 1, 3 and 5 days. (ii) CTS group: freeze-dried CTS scaffolds were placed in the upper chamber and co-cultured with the cells for 1, 3 and 5 days. After culturing, cells were washed with PBS, and then incubated with Calcein and propidium iodide. The staining was observed under the fluorescence microscope. The live (green) and dead (red) MC3T3-E1 cells were evaluated by the live/dead assay. The cell viability was calculated by the following equation: cell viability = [live cells/(live+dead cells)]×100%, (n = 3).

To assess the miRNAs transfection efficacy of CTS NPs, we inoculated the cells at a density of 2×10^5 cells/wall into NPs containing different ratios of load. At the 24-hour and 14-day time points, cells were washed twice with PBS and collected with lysate. The content of miRNA was measured with miDETECT A Track miRNA qRT-PCR Starter Kit (RIBOBIO C10712-1, Guangzhou, China). As the blank control group, cells were subjected to no intervention.

Gel Retardation Analysis

Equal quantities of miR-34c-5p Antagomir were mixed with different ratios of CTS NPs and 2× RNA loading buffer to a 2% agarose gel. The resulting samples were loaded into designated wells along with small RNA ladder (Beyotime, Beijing, China). Gel electrophoresis was conducted using 1× Tris-borate ethylenediaminetetraacetic acid buffer at 110 V for 20 min. Gel imaging system (Bio-Rad, US) was employed to visualize and capture images of the gel. Additionally, both naked miR-34c-5p Antagomir and CTS/miR-34c-5p Antagomir underwent individual incubation with 1 mg/mL RNase A at 37°C for 1 h to evaluate the protective capability of CTS scaffolds.

Measurement of Loading Ratio

The loading ratio of miR-34c-5p Antagomir on CTS scaffolds was determined using a spectrophotometer (Kaiao Technology, Beijing, China). The miR-34c-5p Antagomir was set at a fixed N/P ratio of 20:1 and gently combined with scaffolds featuring different CTS ratios. The initial total amount of miRNAs was recorded as W_0. Subsequently, 10 μL supernatant from centrifugation at 10, 000 rpm for 10 min was extracted from each sample for analysis. The concentration of miRNA was assessed using the RNA detection channel of the spectrophotometer, enabling the determination of the remaining miRNA content (W_1). The loading ratio of CTS scaffolds for miR-34c-5p Antagomir was calculated using the formula: Loading ratio = $(W_0-W_1)/W_0\times100\%$.

Assessment of Release Performance

CTS scaffolds were prepared using the designated volume ratio. To evaluate the release effect of miR-34c-5p from the scaffolds, 250 μL complex was dispensed into the 48-well plate and subjected to freeze-drying. Based on N/P=20:1, the miR-34c-5p Antagomir was added to form the CTS/miR-34c-5p Antagomir complex. The initial total amount of miRNAs was recorded as W_0. Subsequently, the miRNA concentration in the supernatant was measured over a span of 30 days at various time points. The releasing ratio of CTS scaffolds for miR-34c-5p Antagomir was calculated using the formula: Releasing ratio = $W_x/W_0\times100\%$ (X represents the measuring day).

Rabbit Calvarial Bone Formation Induced by CTS Scaffolds

The animal model protocols of this study were approved by the Ethics Committee of Tianjin Stomatological Hospital Ethics Committee (PA2021-B-002). We followed the guideline for ethical review of animal welfare for laboratory animals (GB/T 35892–2018). A total of 16 New Zealand rabbits (aged 3 months and weighed 2.5±0.5 kg) were provided by the Institute of Radiological Medicine of the Chinese Academy Medical Sciences [Animal license number: SCXK (Tianjin) 2021–0001] for feeding and perioperative management.

After 1 week of adaptive feeding, the experimental animals were modeled according to the unified standard. The surgical animals were anesthetized with 2% nasal isoflurane in oxygen, then placed in a prone position on a fixed table, and the limbs and head were fixed. During surgery, a dry heating pad was placed to maintain the animal's body temperature. The operative area was disinfected, and covered with sterile drapes. Copious sterile saline was irrigated to remove debris and to avoid the frictional heat at the surgical site. The bone defects of 4 circular holes were standardised using an 6-mm diameter trephine drill. The wound was closed in layers and disinfected again. The B-type heal mouth rehabilitation membrane (ZH-Bio, Yantai, Shandong, China) was placed over the defect at least 2 mm and under the periosteum. After the operation, the rabbits were injected with 4×10^5 U penicillin intramusculally for 3 consecutive days after operation. The stitches were removed 1 week after operation.

The animals in each group were euthanized by air embolization at 4, 8 and 12 weeks after operation. The cranial parietal bone was trimmed 2 mm away from the defect area to observe the healing of bone defects and fixed with 4% (w/v) paraformaldehyde for 24 h at room temperature.

Micro-CT Scanning Evaluation

The samples were scanned using Micro-CT scanner (Bruker sky scan 1276). The scanning parameters were 85 kV, 200 μA and resolution was 8 μm. All samples were observed and compared in the same mode. After 3D reconstruction of the bone defect image, CT Analyser (1.17.7.2) software was used to evaluate Bone Volume (BV), Tissue Volume (TV) and Bone volume percentage (BV/TV) in the area with the largest defect diameter. BV/TV of each group (n = 4, total 16) was statistically analyzed and compared among the groups. The same measurement index was analyzed three times, and the average value was taken as the final statistical result.

Histological Observations

Following micro-CT scanning, the examples were decalcified in decalcification solution for 2 months and then paraffin-embedded. Subsequently, serial paraffin sections of 5 micrometers in thickness were obtained from the central area of the skull defect using the Leica RM2235 microtome (Leica, Hamburg, Germany). These sections were then stained with

hematoxylin and eosin (H&E) and Masson's trichrome according to the manufacturer's instructions. The stained tissue sections were examined under a Ti-S optical microscope (Nikon, Japan) for detailed analysis.

Statistical Analyses

SPSS Statistic (SPSS Inc., Chicago, IL, USA) was used for statistical analysis. Data were expressed as mean ± standard deviation (SD). All experimental data were analysed by one-way ANOVA and Bonferroni-*t* test. The *P* value less than 0.05 was considered a significant difference in results.

Results

Characterization of CTS/miR-34c-5p Nanoparticles

CTS scaffolds were produced by ionic gelation between positively charged CS and negatively charged STPP. As shown in Figure 1A, CS solution is clear and transparent. After adding STPP and SA, it became translucent. After freeze-drying, the

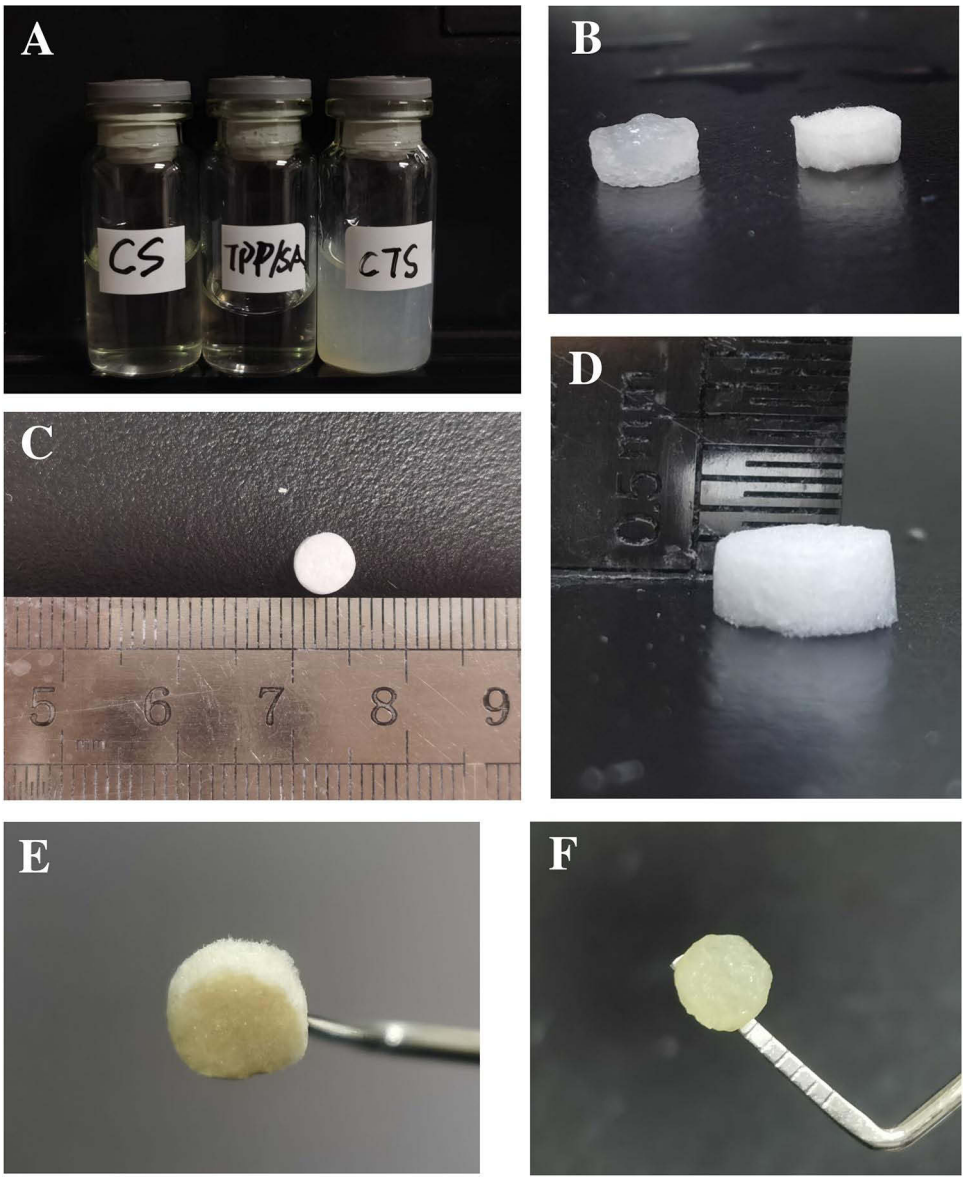

Figure 1 Preparation of CTS scaffolds. (**A**) CS solution and CTS NPs. (**B**) CTS scaffolds in absorbent state (left) and freeze-dried state (right). (**C**) The diameter of CTS scaffolds after freeze-drying in the 96-well plates was 6 mm. (**D**) The height of the CTS scaffolds after freeze-drying in the 96-well plate was 1.5 mm. (**E**) Freeze-dried CTS scaffolds under high temperature and pressure. (**F**) CTS scaffolds with miR-34c-5p Antagomir added after sterilization.

Table 1 Physical Parameters of CTS Scaffolds

CS:STPP:SA	Particle size (nm)	PDI	Zeta potential (mV)
1:0.1:0.02	440.2	0.580	8.89
1:0.2:0.02	260.3	0.474	6.68
1:0.2:0.05	279.1	0.421	7.24
1:0.2:0.1	360.1	0.340	6.72
1:0.2:0.5	370.9	0.380	7.87

scaffold with absorbing water did not collapse or loosen, and slightly expanded (Figure 1B). Meanwhile, the complex with equal amount in a 96-well plate can be formed to cylindrical scaffolds with a diameter of 6 mm and a height of 1.5 mm (Figure 1C and D). After sterilization at 110°C, the colour of scaffolds changed from white to light yellow (Figure 1E). After adding miR-34c-5p Antagomir, the complex showed jelly-like luster (Figure 1F).

The physical and chemical parameters of CTS NPs were shown in Table 1. The dispersion of CTS NPs was appropriate. The particle size and Zeta potential were determined by the volume ratio among CS, STPP and SA. With the increasing of SA ratio, the particle size of CTS increased from 260.3 nm to 370.9 nm, while the Zeta potential did not change significantly. The PDI value of CTS NPs was the smallest when the ratio of CS/STPP/SA reached 1:0.2:0.1. It indicated that the NPs prepared with this ratio had the most uniform particle size distribution. At this time, CTS NPs have the suitable particle size (360.1 nm) and potential (6.72 mV), and this ratio will be selected for the subsequent study.

With the increase of SA concentration, the swelling rate increased. However, it had no significantly change with the increasing of STPP ratio (Figure 2A). The porosity results are shown in Figure 2B. Within the set volume ratio range, the porosity tended to raise with the increasing of SA proportion. When the ratio of CS/STPP/SA reached 1:0.2:0.1, the porosity remained stable at about 79.32%.

The surface morphologies of CTS/miR-34c-5p scaffolds were photographed by SEM. The results showed that the freeze-dried scaffolds had loose and porous spongy structures. At high magnification, the spaces between the spongy structures could be connected (Figure 3A). The sample measured in this study presented an average diameter of 200–300 nm (Figure 3B). SEM showed that MC3T3-E1 could adhere to the surface of the scaffold, and the cells were polygonal in shape and had protrusions (Figure 3C).

The binding capacity of CTS NPs with miR-34c-5p Antagomir was confirmed by the gel retardation assay. As shown in Figure 4A, various proportions of CTS NPs had inconsistent loading effects on miR-34c-5p Antagomir. When the ratio of CS/STPP/SA reached 1:2:0.05, CTS achieved the best retarding effect. Meanwhile, bare miR-34c-5p Antagomir could be partially degraded after incubation at 37°C by 1 mg/mL RNase A for 1 h. When the ratio of CS/STPP/SA reached

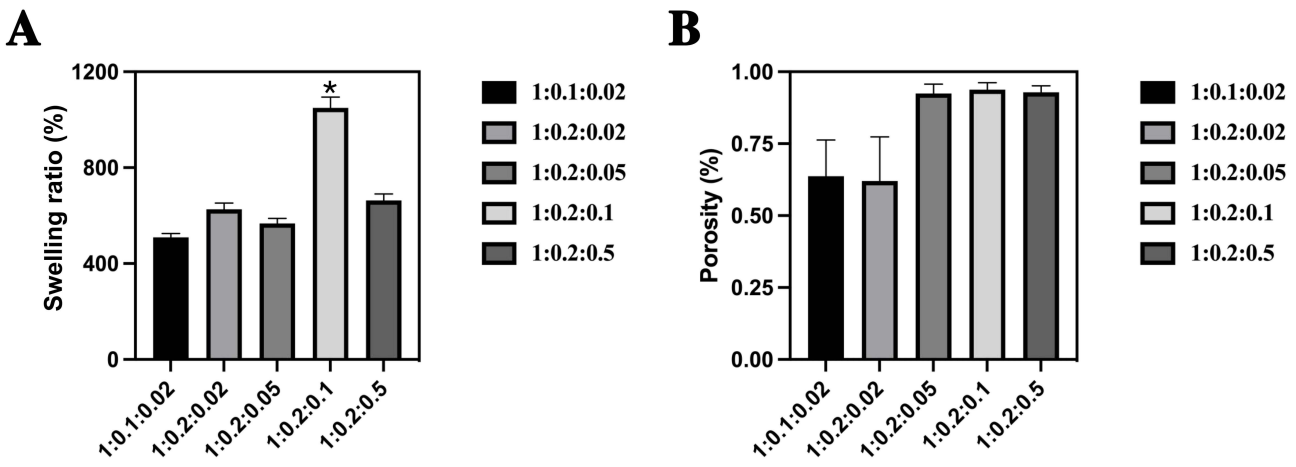

Figure 2 Characterization of CTS/miR-34c-5p Nanoparticles. (**A**) The swelling ratio of CTS NPs with different ratios (*$P < 0.05$). (**B**) The porosity of CTS NPs with different ratios.

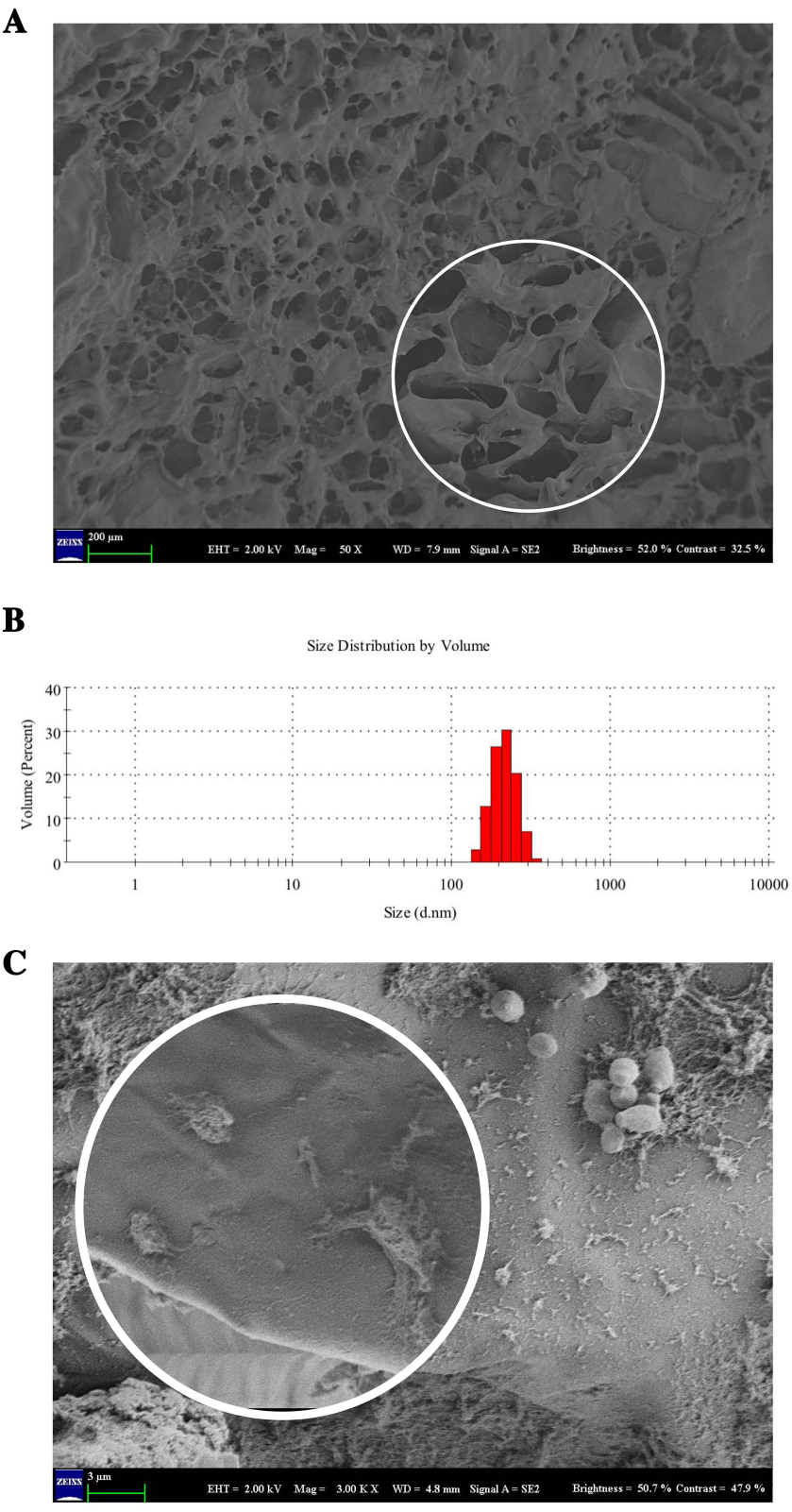

Figure 3 Physicochemical properties of CTS scaffolds. (**A**) SEM view of CTS scaffolds (100× magnification for circular SEM illustrations). (**B**) Particle size distribution. (**C**) SEM view of MC3T3-E1 cells cultured on the scaffold (1.5× magnification for circular SEM illustrations).

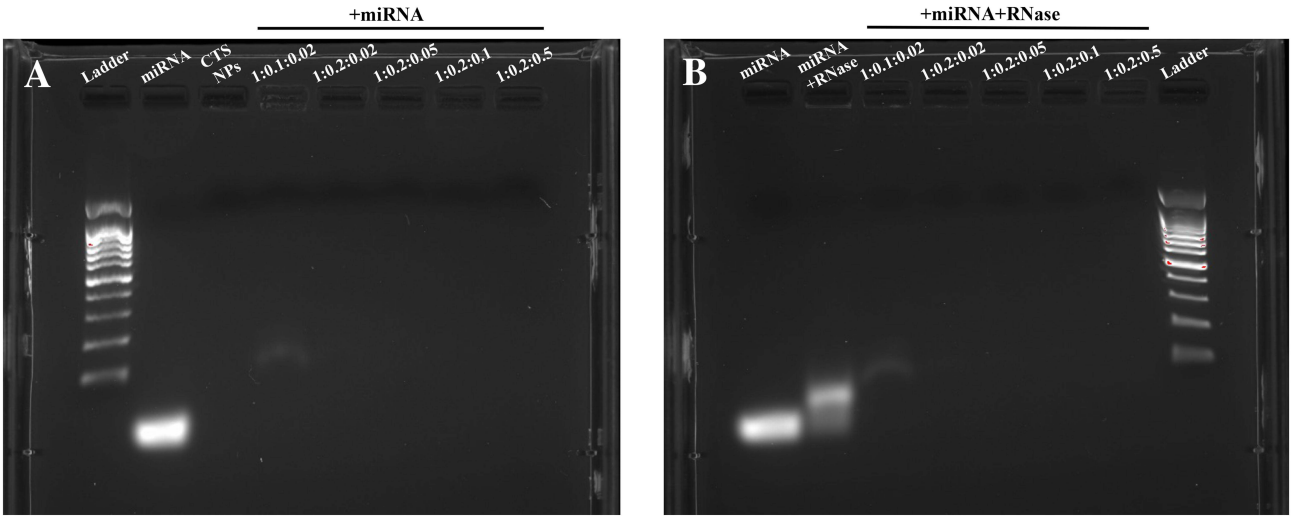

Figure 4 Gel Retardation Analysis. (**A**) Gel electrophoresis of different CTS ratios loaded with miR-34c-5p Antagomir. (**B**) Gel electrophoresis of NPs loaded with miR-34c-5p Antagomir underwent incubation with RNase A.

1:0.1:0.02, miR-34c-5p Antagomir were remained in the lane. When the ratio of CS/STPP/SA reaches 1:0.2:0.05, there was no miR-34c-5p Antagomir in the loading lane (Figure 4B). The results indicated that miR-34c-5p Antagomir could not be degraded by RNase A, which proved that CTS NPs could resist the degradation of RNase A.

Cytotoxicity and Transfection Efficiency of CTS/miR-34c-5p NPs

The cytotoxicity of different substrates was assessed by a live/dead cell staining kit activity in the culture media after 24 hours of transfection. As shown in Figure 5, after 1, 3 and 5 days of co-culture, the vast majority of cells remained viable. No obvious cytotoxicity were observed between groups ($P>0.05$). QRT-PCR Starter Kit was employed to evaluate the transfection efficacy in cells after transfection for 24 hours and 14 days (Figure S1). The results indicated that different CTS ratio induced different transfection efficacies. In total, every ratio efficacy increased the transfection efficacies over the observation time.

Loading and Release Rates

The loading efficiency of miR-34c-5p Antagomir in CTS scaffolds increased from 45.67% (at a ratio of 1:0.1:0.02) to 90.13% (at a ratio of 1:0.2:0.05) with the rising proportion of STPP and SA. Further adjustments in the SA ratio showed negligible impact on the loading capacity of miR-34c-5p Antagomir (Figure 6).

Regarding the slow-release pattern, initial measurements on Day 1 were followed by assessments every two days until 30 days. The findings demonstrated the obvious burst releasing of miR-34c-5p Antagomir within the first 10 days, accounting for 53.4% of the total content. By Day 22, the cumulative releasing reached 83.92%. And by Day 30, it reached 91.41%, which indicated that the scaffolds had the better-sustained release capacity in miRNAs (Figure 7).

Effects of miR-34c-5p on Bone Defect Repair and Healing in vivo

The experimental procedure was shown in Figure 8. A longitudinal incision was made along the midline of the skull, about 5 cm long and full-thickness to the calvaria (Figure 8A). The bone defects were standardised using an 6-mm diameter trephine drill to outline the treatment area in each of the four quadrants in all animals (Figure 8B–G). The groups were transplanted into the defect area of the rabbit calvarial bone and placed clockwise from the lower right hole at the head of the animal: (i) sham operation group (Blank), (ii) The empty Vector group (Vector), (iii) CTS/miR-34c-5p Agomir group, (iv) CTS/miR-34c-5p Antagomir group.

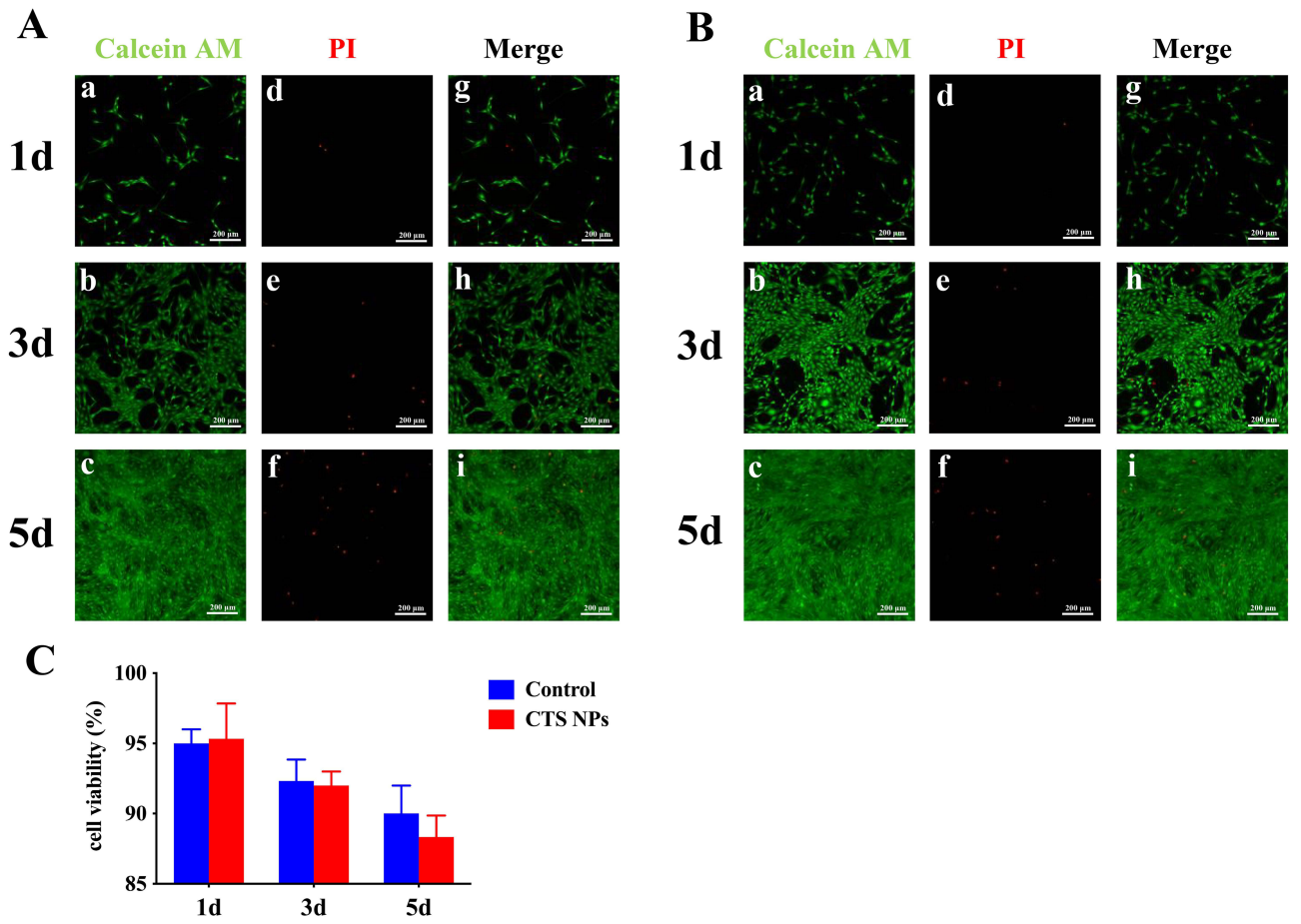

Figure 5 The activity of MC3T3-E1 cells was detected by double fluorescence staining. (**A**) Representative images of MC3T3-E1 stained by Calcein-AM/PI in the Control group (bar = 200 μm). (**B**) Representative images of MC3T3-E1 stained by Calcein-AM/PI in the CTS NPs group (bar = 200 μm). (**C**) Statistical analysis of MC3T3-E1 survival rate by Calcein-AM/PI staining.

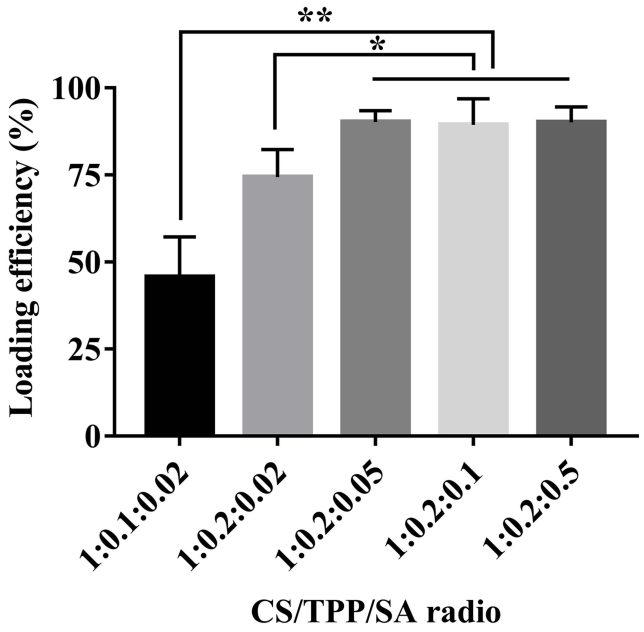

Figure 6 The loading ratio of CTS scaffolds on miR-34c-5p Antagomir (*P < 0.05; **P < 0.01).

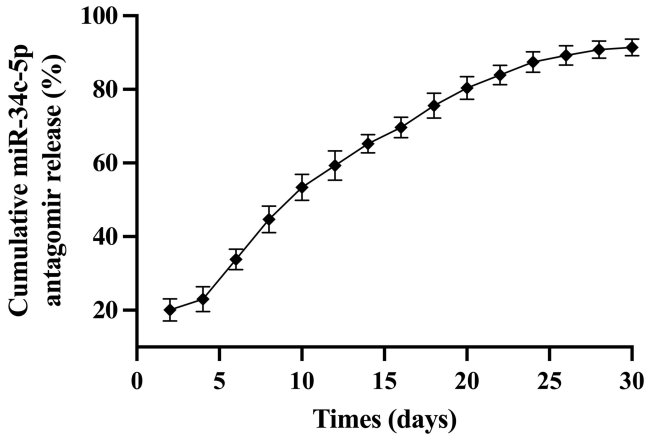

Figure 7 Assessment of Release Performance.

Rabbits were killed at 4, 8 and 12 weeks, respectively. No epidural hematoma or effusion was observed. General observation showed four defect areas of cranial parietal bone were all depressed and covered with fibrous connective tissue (Figure 9). The samples from each group had different degree of new bone formation.

After scanning, the three-dimensional (3D) images were reconstructed using CT vox 3D reconstruction software (3.3.0) (Figure 10A). The defect area of cranial parietal bone was selected as the Region of interest (ROI) (Figure 10B). After VT vox 3D reconstruction, all groups showed different degree of bone repair. As time going, the bone defect gradually diminished and the amount of new bone production gradually increased. As shown in the micro-CT results, notable new bone formation was observed within the 6-mm defect area in the Antagomir group at both 4, 8 and 12 weeks post-surgery ($P < 0.05$). Quantitative statistics were carried out to calculate the newly formed bone (NFB) of each group (Figure 11). Significant differences were observed in Antagomir group versus control and Agomir group at both 4, 8 and 12 weeks ($P < 0.05$).

Bone healing was also evaluated in the H&E and Masson's trichrome staining sections. Through the Masson staining, we observed the larger area of NFB which contained more fibrous connective tissue and neovascularization (Figure 12) in the Antagomir versus Agomir groups. The results showed that miR-34c-5p Antagomir does affect bone defect repair in vivo.

Discussion

MiRNAs play a pivotal role in bone remodeling processes. MiRNAs-based non-cellular therapy is an emerging strategy that can avoid potential side effects of traditional cell therapy, including immune rejection and biological incompatibility, as well as following high expense.[24] To address the challenges faced in efficiently delivering miRNAs, it is imperative to identify an appropriate scaffold capable of carrying miRNAs specifically targeted to bone tissue. This scaffold would serve as a vehicle for the miRNAs, ensuring precise delivery and enhancing therapeutic efficacy in bone remodeling applications.

Based on these, in this study, we designed CS/STPP/SA scaffolds loaded with miR-34c-5p and applied to the rabbit cranio-parietal defect model to evaluate its osteogenic effect. We conducted a comprehensive characterization of the nanoparticles, including measurements of particle size, morphology, and Zeta potential distribution. Cytotoxicity, loading efficiency, and release rates were also evaluated to provide a reference for subsequent in vivo experiments, thus demonstrating the feasibility of these scaffolds for cell-free therapy applications. Among these measurements, the assessment of Zeta potential was particularly crucial for determining the surface charge properties of the particles. Our results revealed that the particle size increased significantly with a higher ratio of SA. The Zeta potential ranged between +6 mV and +8 mV, primarily due to the presence of free amino groups on the surface of CS. These positive charges facilitated interactions with negatively charged cell membranes, enhancing the potential for effective delivery and cellular internalization of the miR-34c-5p loaded scaffolds.[25]

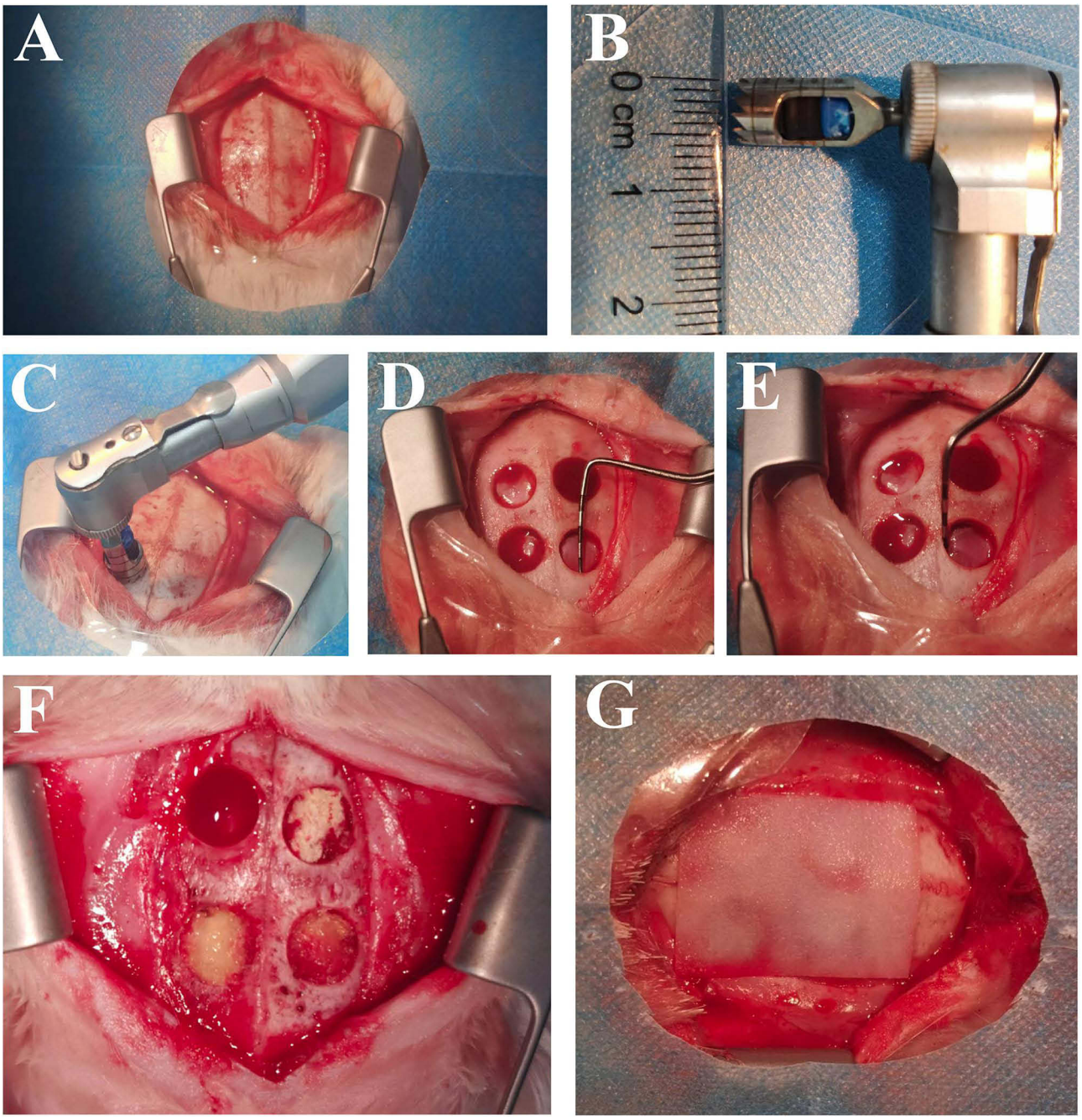

Figure 8 Experimental animal surgery procedure. (**A**) Exposed surgical area. (**B**) Diameter of trephine drill. (**C**) Surgical localization. (**D**) Diameter of bone defect. (**E**) Depth of bone defect. (**F**) Implant contents in each group. (**G**) Cover B-type heal mouth rehabilitation membrane.

SEM imaging revealed the porous and interconnected structure within the CS/STPP/SA scaffolds, which is crucial for cell infiltration and angiogenesis.[26] Interconnectivity and porosity are well-recognized factors that contribute to the effectiveness of scaffolds in tissue engineering applications. Polymeric scaffolds have been shown to enhance the mechanical properties of cartilage matrix and improve its osteogenic differentiation potential.[27,28] Our findings further suggested that higher ratios of SA in the scaffolds could improve porosity, creating a more conducive environment for cell proliferation. This is the significant observation as porosity serves as a key performance index for composite materials in tissue engineering.[29] Additionally, gel retardation analysis confirmed that the miRNAs remained within the agarose gel pores, demonstrating the binding capacity of miR-34c-5p to the CTS scaffolds. This binding capacity is

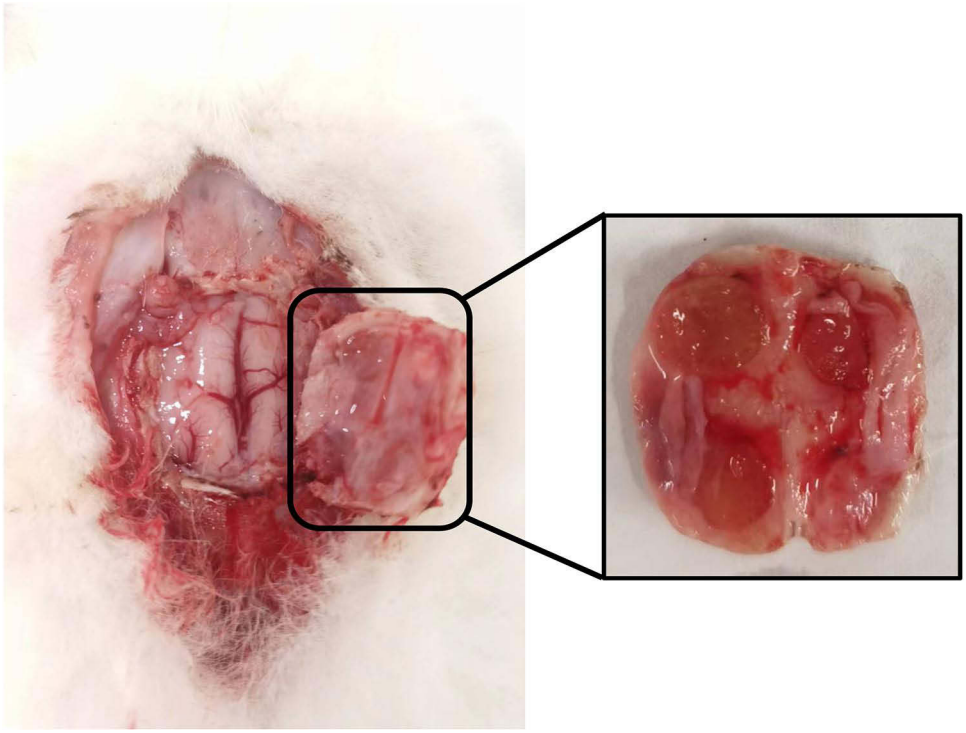

Figure 9 Specimen observation.

essential for the effective delivery and retention of miRNAs at the target site, enhancing their therapeutic potential in bone remodeling applications. Overall, these results support the feasibility and effectiveness of the designed CS/STPP/SA scaffolds loaded with miR-34c-5p for cell-free therapy applications.

We also co-cultured MC3T3-E1 cells with the CTS scaffolds to assess the biocompatibility of the complex. It was observed in our study, as well as other studies, that CTS scaffolds had negligible cytotoxicity to MC3T3-E1 cells.[30] It was well established that the toxicity of nanomaterials can arise from their nano-size effect, which increased their chemical reactivity due to larger specific surface area.[31] This reactivity can lead to the rapid generation of reactive oxygen species and free radicals, potentially inducing oxidative stress, inflammatory responses, protein denaturation, and DNA damage.[32] Therefore, it is crucial to strike a balance between achieving the desired nano-size for effective delivery and minimizing potential toxicity. Our scaffold has been well-characterised in vitro in terms of its physical properties, microstructure and cyto-compatibility.

Furthermore, we successfully established four 6 mm full-layer cranial parietal bone defects in each New Zealand rabbit, with the repair duration of 4, 8 and 12 weeks. No adverse reactions were observed post-implantation. The tissue sections revealed varying degrees of new bone formation in each group after 4, 8 and 12 weeks of post-surgery. Histochemical staining was employed to visualize collagen fibers, cytoplasm, keratin and erythrocytes, indicating superior osteogenesis effect of Antagomir over the Vector group at different time points. These outcomes suggested that miR-34c-5p-loaded scaffolds are able to regulate bone repairs in defect areas.

The observations at different time points provide valuable insights into the degradation and osteogenic properties of the scaffolds. The micro-CT and histological analyses revealed findings regarding the healing process in the different groups. At 4 weeks, the scaffolds remained intact and provided channels for osteoblast colonization, which is crucial for the initiation of bone regeneration. By 8 and 12 weeks, varying degrees of scaffold degradation were observed, coinciding with new bone tissue and marrow space formation. Specifically, the Agomir group showed slower healing process compared to the Vector group, while the Antagomir group exhibited relatively accelerated bone healing, particularly by 12 weeks. These results suggest that the miR-34c-5p loaded scaffolds have the regulatory effect on bone healing, with the Antagomir group demonstrating a more favorable outcome. However, it is important to note that there was no significant difference in bone repair between the Blank group and the Vector group. This suggests that the scaffolds do not have an additional impact on bone defect repair.

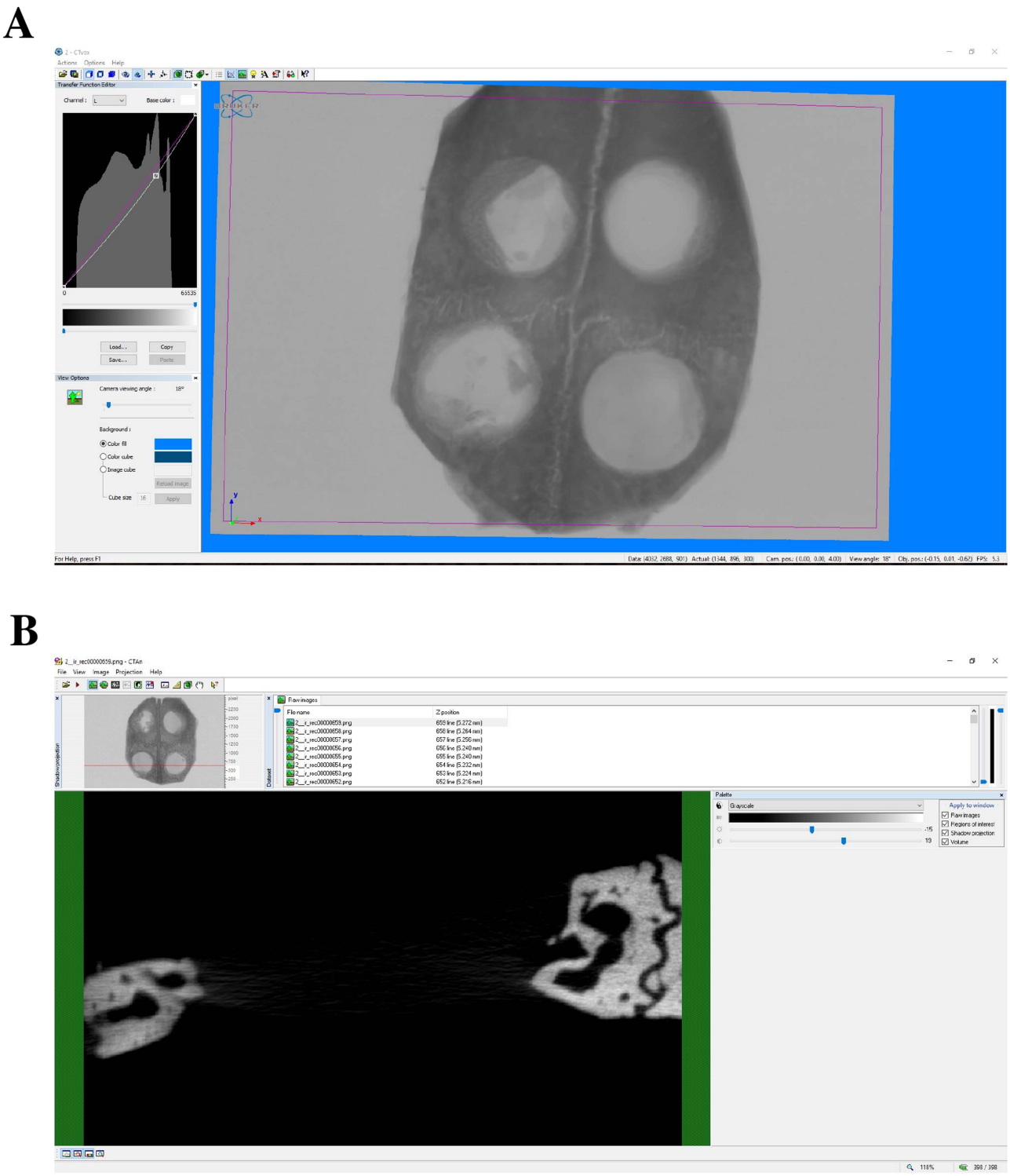

Figure 10 Software analysis interface. (**A**) CT vox 3D reconstruction. (**B**) CT Analyser for bone Bone Volume percentage analysis.

Masson staining shows an intuitive representation of the collagen content and organization within the bone tissue.[33] During the transition from new to mature bone, osteoblasts secrete type I collagen, which is stained blue by Masson staining. This blue staining indicates the presence of newly formed bone tissue and collagen fibers.[34] As the bone tissue matures, the collagen fibers undergo a gradual transformation into type II collagen, imparting the red hue to mature bone.[35]

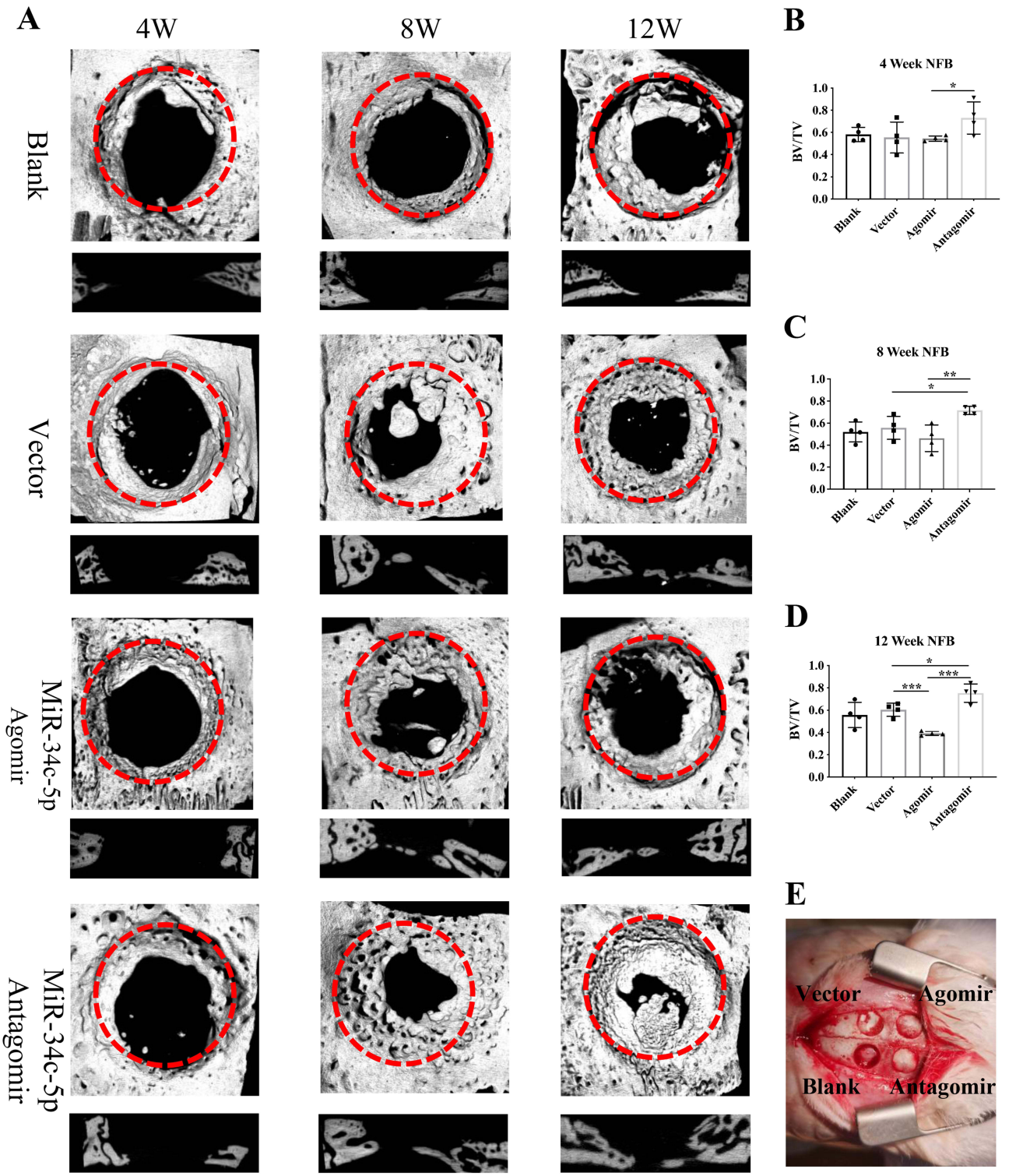

Figure 11 Regulation of miR-34c-5p on bone defect healing in vivo. (**A**) Micro-CT images of full-layer cranial parietal bone regeneration in New Zealand white rabbits at 4, 8, and 12 weeks after surgery. The red dashed circles represent the boundary of the bone defect. (**B-D**) The relative bone volume fraction of New forming bone (NFB) was quantitatively analyzed (*P < 0.05; **P < 0.01; ***P < 0.001). (**E**) Schematic diagram of group preparation.

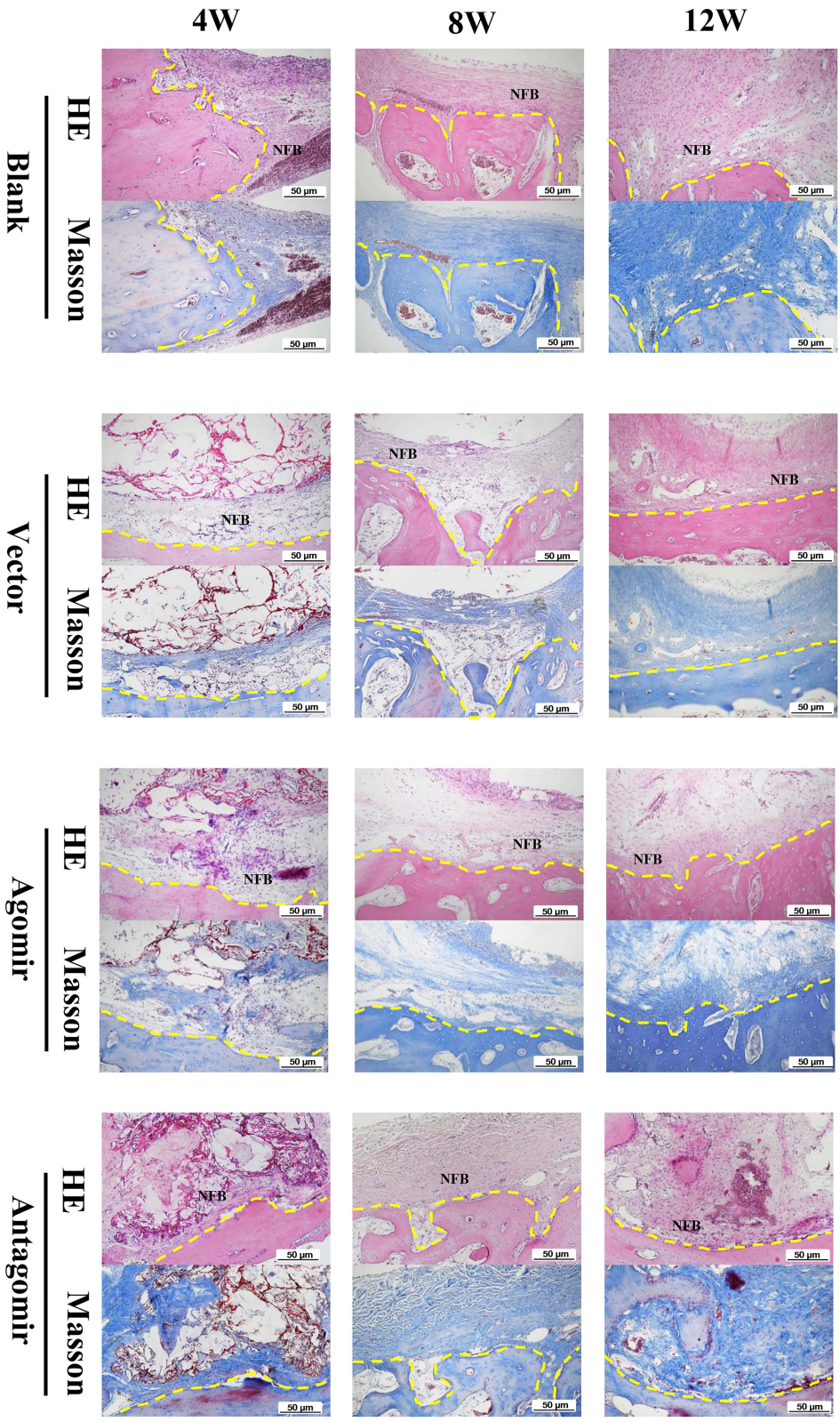

Figure 12 HE and Masson staining on rabbit cranio-parietal defect repair at 4, 8 and 12 weeks after surgery. The yellow dashed lines represent the boundary of the bone defect (NFB: New forming bone, bar = 50 μm).

An irregular extension was observed toward the central defect area of new bone in the Blank group, consistent with Xu et al's findings on guided bone regeneration technology.[36] Conversely, the Antagomir group exhibited abundant new bone generation at both central and marginal defect locations. New bone initially appears at the border area of defect, undergoing calcification gradually. The research by Yu Wei et al provides a plausible explanation for the slow bone formation observed in the central defect area. Specifically, they suggested that poor blood flow and less regenerative vascularization in the central defect area may limit the formation of new collagen fibers, cells, and bone trabeculae.[37]

To our knowledge, this study is the first to emphasize the significant impact of miR-34c-5p on bone formation in rabbit cranio-parietal defects. MiRNAs, as small RNA molecules that regulate gene expression in vivo, hold extensive utility in identifying gene functions and diagnosing diseases.[38] However, RNA therapy has consistently faced challenges, such as RNA degradation and the inability to sustain effective working concentrations within cells.[39] Our findings indicate that scaffolds loaded with miRNAs can effectively influence bone remodeling, thereby offering a potential solution for applications in bone tissue engineering.[40]

Nevertheless, there still exists some limitations in our study. First, the bone repair processes observed in our experimental animals differ significantly from those in humans. Therefore, subsequent research, including experiments on the pharmacokinetics and mechanisms of miRNAs, is imperative to validate the feasibility and efficacy of scaffolds loaded with miRNAs, ultimately paving the way for their clinical application. Second, while our findings highlight the crucial role of miR-34c-5p in regulating bone repair, there are still other vital mechanisms involved in the bone remodeling process that require further investigation. Given their widespread presence as endogenous non-coding RNA in the human body, miRNAs will undoubtedly play a pivotal role in disease diagnosis and treatment in the future.

Conclusion

In this study, we have developed CTS scaffolds as the nonviral carrier for miRNA delivery. The scaffolds were not only loaded with miRNAs but also avoid miRNAs from degradation by RNase. The assay results demonstrated the CTS scaffolds did not show any significant cytotoxicity on MC3T3-E1. Moreover, in vivo experiments miR-34c-5p could regulate the osteogenic process of cranial parietal defects in rabbits. These findings might thus provide the novel strategy that chitosan-based scaffolds may be an effective non-viral vector for the related treatment of bone defects. It will also provide an innovative solution for bone defects in future clinical applications.

Abbreviations

miRNAs, microRNAs; CS, Chitosan; CSD, critical-sized defect; STPP, Sodium tripolyphosphate; SA, Sodium alginate; SEM, scanning electron microscopy; NPs, nano-particles; CTS, Chitosan/Sodium tripolyphosphate/Sodium alginate; PDI, polymer dispersity index; ROI, Region of interest; BV, Bone Volume; TV, Tissue Volume; H&E, Hematoxylin and eosin; SD, standard deviation; NFB, newly formed bone.

Acknowledgments

This work is funded by Tianjin Key Medical Discipline (Specialty) Construction Project [TJYXZDXK-024A] and [ZJZX202202] and Tianjin Health Research Project (TJWJ2024XK019). We also thank Zheng Hong, Kai Chen, and Haitao Chen for their brilliant technical assistance.

Disclosure

The authors declare no competing financial interest in this work.

References

1. Shao J, Pan T, Wang J, et al. MiR-208b Regulates Rabbit Preadipocyte Proliferation and Differentiation. *Genes*. 2021;12(6). doi:10.3390/genes12060890
2. Yang M, Gao X, Ma Y, et al. Bta-miR-6517 promotes proliferation and inhibits differentiation of pre-adipocytes by targeting PFKL. *J Anim Physiol Anim Nutr*. 2022;106(6):1197–1207. doi:10.1111/jpn.13662
3. Zhu Y, Li P, Dan X, Kang X, Ma Y, Shi Y. miR-377 Inhibits Proliferation and Differentiation of Bovine Skeletal Muscle Satellite Cells by Targeting FHL2. *Genes*. 2022;13(6). doi:10.3390/genes13060947

4. Yang F, Zhang X, Song T, et al. Huogu injection alleviates SONFH by regulating adipogenic differentiation of BMSCs via targeting the miR-34c-5p/MDM4 pathway. *Gene*. 2022;838:146705. doi:10.1016/j.gene.2022.146705
5. Hao Y, Ge Y, Li J, Hu Y, Wu B, Fang F. Identification of MicroRNAs by Microarray Analysis and Prediction of Target Genes Involved in Osteogenic Differentiation of Human Periodontal Ligament Stem Cells. *J Periodontol*. 2017;88(10):1105–1113. doi:10.1902/jop.2017.170079
6. Luan X, Zhou X, Trombetta-eSilva J, et al. MicroRNAs and Periodontal Homeostasis. *J Dent Res*. 2017;96(5):491–500. doi:10.1177/0022034516685711
7. Wang Q, Shen X, Chen Y, Chen J, Li Y. Osteoblasts-derived exosomes regulate osteoclast differentiation through miR-503-3p/Hpse axis. *Acta Histochem*. 2021;123(7):151790. doi:10.1016/j.acthis.2021.151790
8. Lin C, Yang Y, Wang Y, et al. Periodontal ligament fibroblasts-derived exosomes induced by PGE2 inhibit human periodontal ligament stem cells osteogenic differentiation via activating miR-34c-5p/SATB2/ERK. *Exp Cell Res*. 2022;419(2):113318. doi:10.1016/j.yexcr.2022.113318
9. Kharaghani D, Kurniwan EB, Khan MQ, MiRNA-Nanofiber YY. the Next Generation of Bioactive Scaffolds for Bone Regeneration: a Review. *Micromachines*. 2021;12(12). doi:10.3390/mi12121472
10. Tong Y, Lee Y, Liu X, et al. Programming inactive RNA-binding small molecules into bioactive degraders. *Nature*. 2023;618(7963):169–179. doi:10.1038/s41586-023-06091-8
11. Karagkouni D, Karavangeli A, Paraskevopoulou MD, Hatzigeorgiou AG. Characterizing miRNA-lncRNA Interplay. *Methods Mol Biol*. 2021;2372:243–262. doi:10.1007/978-1-0716-1697-0_21
12. Sui L, Wang M, Han Q, et al. A novel Lipidoid-MicroRNA formulation promotes calvarial bone regeneration. *Biomaterials*. 2018;177:88–97. doi:10.1016/j.biomaterials.2018.05.038
13. Lee S, Paoletti C, Campisi M, et al. MicroRNA delivery through nanoparticles. *J Control Release*. 2019;313:80–95. doi:10.1016/j.jconrel.2019.10.007
14. Gan K, Dong GH, Wang N, Zhu JF. miR-221-3p and miR-222-3p downregulation promoted osteogenic differentiation of bone marrow mesenchyme stem cells through IGF-1/ERK pathway under high glucose condition. *Diabet Res Clin Pract*. 2020;167:108121. doi:10.1016/j.diabres.2020.108121
15. Wu S, Zhang H, Wang S, et al. Ultrasound-triggered in situ gelation with ROS-controlled drug release for cartilage repair. *Mater Horiz*. 2023;10(9):3507–3522. doi:10.1039/d3mh00042g
16. Fakhri E, Eslami H, Maroufi P, et al. Chitosan biomaterials application in dentistry. *Int J Biol Macromol*. 2020;162:956–974. doi:10.1016/j.ijbiomac.2020.06.211
17. Wu N, Zhang X, Li J, Gan Y. Targeting exosomal miRNA with pH-sensitive liposome coated chitosan-siRNA nanoparticles for inhibition of hepatocellular carcinoma metastasis. *J Control Release*. 2015;213:e82. doi:10.1016/j.jconrel.2015.05.136
18. Ashrafizadeh M, Hushmandi K, Mirzaei S, et al. Chitosan-based nanoscale systems for doxorubicin delivery: exploring biomedical application in cancer therapy. *Bioeng Transl Med*. 2023;8(1):e10325. doi:10.1002/btm2.10325
19. Hu C, Zhang L, Wei M. Development of Biomimetic Scaffolds with Both Intrafibrillar and Extrafibrillar Mineralization. *ACS Biomater Sci Eng*. 2015;1(8):669–676. doi:10.1021/acsbiomaterials.5b00088
20. Nunes R, Serra AS, Simaite A, Â S. Modulation of Chitosan-TPP Nanoparticle Properties for Plasmid DNA Vaccines Delivery. *Polymers*. 2022;14(7). doi:10.3390/polym14071443
21. Chatelet M, Afota F, Savoldelli C. Review of bone graft and implant survival rate: a comparison between autogenous bone block versus guided bone regeneration. *J Stomatol Oral Maxillofac Surg*. 2022;123(2):222–227. doi:10.1016/j.jormas.2021.04.009
22. Rashtbar M, Hadjati J, Ai J, et al. Critical-sized full-thickness skin defect regeneration using ovine small intestinal submucosa with or without mesenchymal stem cells in rat model. *J Biomed Mater Res B Appl Biomater*. 2018;106(6):2177–2190. doi:10.1002/jbm.b.34019
23. Bahraminasab M, Talebi A, Doostmohammadi N, Arab S, Ghanbari A, Zarbakhsh S. The healing of bone defects by cell-free and stem cell-seeded 3D-printed PLA tissue-engineered scaffolds. *J Orthop Surg Res*. 2022;17(1):320. doi:10.1186/s13018-022-03213-2
24. Wang G, Yuan Z, Yu L, et al. Mechanically conditioned cell sheets cultured on thermo-responsive surfaces promote bone regeneration. *Biomater Transl*. 2023;4(1):27–40. doi:10.12336/biomatertransl.2023.01.005
25. Pooja D, Babu Bikkina DJ, Kulhari H, et al. Fabrication, characterization and bioevaluation of silibinin loaded chitosan nanoparticles. *Int J Biol Macromol*. 2014;69:267–273. doi:10.1016/j.ijbiomac.2014.05.035
26. Harley BA, Kim HD, Zaman MH, Yannas LDA IV, Gibson LJ. Microarchitecture of three-dimensional scaffolds influences cell migration behavior via junction interactions. *Biophys J*. 2008;95(8):4013–4024. doi:10.1529/biophysj.107.122598
27. Giannotti L, Di Chiara Stanca B, Nitti P, et al. Hydroxyapatite-Silicon Scaffold Promotes Osteogenic Differentiation of CGF Primary Cells. *Biology*. 2023;12(4). doi:10.3390/biology12040528
28. Lu G, Xu Y, Liu Q, et al. An instantly fixable and self-adaptive scaffold for skull regeneration by autologous stem cell recruitment and angiogenesis. *Nat Commun*. 2022;13(1):2499. doi:10.1038/s41467-022-30243-5
29. Ouyang L, Yao R, Zhao Y, Sun W. Effect of bioink properties on printability and cell viability for 3D bioplotting of embryonic stem cells. *Biofabrication*. 2016;8(3):035020. doi:10.1088/1758-5090/8/3/035020
30. Dhandapani RK, Gurusamy D, Howell JL, Palli SR. Development of CS-TPP-dsRNA nanoparticles to enhance RNAi efficiency in the yellow fever mosquito, Aedes aegypti. *Sci Rep*. 2019;9(1):8775. doi:10.1038/s41598-019-45019-z
31. Li X, Hu Z, Ma J, et al. The systematic evaluation of size-dependent toxicity and multi-time biodistribution of gold nanoparticles. *Colloids Surf B Biointerfaces*. 2018;167:260–266. doi:10.1016/j.colsurfb.2018.04.005
32. Collins A, El Yamani N, Dusinska M. Sensitive detection of DNA oxidation damage induced by nanomaterials. *Free Radic Biol Med*. 2017;107:69–76. doi:10.1016/j.freeradbiomed.2017.02.001
33. Xiao Z, Fu D, Zhang L, Fan W, Shen X, Qi X. Bone healing study of alendronate combined with enoxaparin sodium bone cement in rabbits with bone defects. *J Orthop Surg Res*. 2022;17(1):431. doi:10.1186/s13018-022-03330-y
34. Yabe Y, Hagiwara Y, Ando A, et al. Chondrogenic and fibrotic process in the ligamentum flavum of patients with lumbar spinal canal stenosis. *Spine*. 2015;40(7):429–435. doi:10.1097/BRS.0000000000000795
35. Lim HP, Mercado-Pagan AE, Yun KD, et al. The effect of rhBMP-2 and PRP delivery by biodegradable β-tricalcium phosphate scaffolds on new bone formation in a non-through rabbit cranial defect model. *J Mater Sci Mater Med*. 2013;24(8):1895–1903. doi:10.1007/s10856-013-4939-9
36. Hung IH, Yu K, Lavine KJ, Ornitz DM. FGF9 regulates early hypertrophic chondrocyte differentiation and skeletal vascularization in the developing stylopod. *Dev Biol*. 2007;307(2):300–313. doi:10.1016/j.ydbio.2007.04.048

37. Yu W, Zhong L, Yao L, et al. Bone marrow adipogenic lineage precursors promote osteoclastogenesis in bone remodeling and pathologic bone loss. *J Clin Invest*. 2021;131(2). doi:10.1172/JCI140214
38. Khatri N, Rathi M, Baradia D, Trehan S, Misra A. In vivo delivery aspects of miRNA, shRNA and siRNA. *Crit Rev Ther Drug Carrier Syst*. 2012;29(6):487–527. doi:10.1615/critrevtherdrugcarriersyst.v29.i6.20
39. Yan Y, Liu XY, Lu A, Wang XY, Jiang LX, Wang JC. Non-viral vectors for RNA delivery. *J Control Release*. 2022;342:241–279. doi:10.1016/j.jconrel.2022.01.008
40. Zhang Y, Wang Z, Gemeinhart RA. Progress in microRNA delivery. *J Control Release*. 2013;172(3):962–974. doi:10.1016/j.jconrel.2013.09.015